

# Facile Fabrication of Multifunctional Aramid Nanofiber Films by Spin Coating

Jing Lyu, Lehao Liu, Xing Zhao, Yudong Shang, Tingkai Zhao, and Tiehu Li

(Submitted June 1, 2016; in revised form July 25, 2016; published online September 28, 2016)

Polymer matrices with excellent mechanical properties, thermal stability and other features are highly demanded for the effective utilization within nanocomposites. Here, we fabricate free-standing aramid nanofiber films via spin coating of an aramid nanofiber/dimethyl sulfoxide solution. Compared with traditional film fabrication methods, this process is time-saving and also able to easily tune the thickness of the films. The resultant films show greatly improved stretchability than that of Kevlar threads and relatively high mechanical strength. Typically, these films with a thickness of 5.5  $\mu\text{m}$  show an ultimate strength of 182 MPa with an ultimate tensile strain of 10.5%. We also apply a finite element modeling to simulate the strain and strength distributions of the films under uniaxial tension, and the results of the simulation are in accordance with the experimental data. Furthermore, the aramid nanofiber films exhibit outstanding thermostability (decomposition at  $\sim 550$  °C under  $\text{N}_2$  atmosphere and  $\sim 500$  °C in air) and chemical inertness, which would endure acid and alkali. The simple method demonstrated here provides an important way to prepare high-performance aramid nanofiber films for designing new composite systems.

**Keywords** aramid nanofiber, chemical stability, finite element modeling, mechanical strength, spin coating, thermal property

## 1. Introduction

Nanocomposites composed of polymer matrices and inorganic fillers have attracted significant attention, because of their promising applications in LED interconnects, sensors, energy-storage devices, etc. (Ref 1-4). The design of high-performance nanocomposites is usually focused on improving the properties of reinforcement phases [such as nanotubes, graphene, nanofibers and inorganic nanoparticles (Ref 5-9)]. The interfacial properties between the reinforcement phases and the matrices have also been extensively studied. For example, the effective load transfer from the matrices to the fillers is essential to reduce stress localization and thus improves the integrated mechanical properties (Ref 10). Moreover, the polymeric matrices with excellent mechanical properties, and other functions such as thermal stability and chemical resistance, are also required to fulfill the design of high-performance nanocomposites.

The present extensively studied polymeric matrices for nanocomposites include polyurethanes (PU) (Ref 11), epoxy (Ref 12) and polymethyl methacrylate (PMMA) (Ref 13). However, these matrices suffer from overall low mechanical

properties especially in stiffness and strength. Cellulose materials can self-assemble into well-defined architectures in multiple scales, from micro- to nanosize and can form networks with high mechanical performance. However, hydrophilic behavior of cellulose makes them very sensitive to humidity, which is attributed to the hydroxyl groups that are located on the surface of the cellulose fibers, reducing their mechanical performance at high humidity (Ref 14).

Aramid fibers, most commonly known as Kevlar, consist of long molecular chains produced from poly(p-phenylene terephthalamide) (PPTA) probably have been considered as a suitable matrix material. Kevlar has numerous applications, ranging from bicycle tires and racing sails to body armor, because of its high tensile strength-to-weight ratio with a high thermal resistance and chemical inertness (Ref 15-17). Kevlar has also been used in composite materials to reinforce other high-ductility, low-stiffness polymers like phenolic and bis-maleimide (Ref 18, 19). However, the macroscale of the commercial aramid fibers limits their applications in nanocomposites. Since the discovery of stable aramid nanofiber (ANF) dispersion through dissolving Kevlar in dimethyl sulfoxide/potassium hydroxide solutions by Kotov group (Ref 20), there are some interesting works on the ANF-modified CNTs which were used to reinforce other polymers (Ref 21). ANFs have also rapidly become widely used polymeric matrices with attractive properties for many new ANF-based composite films like PU/ANF nanocomposites and graphene/ANF nanocomposites (Ref 22-29). In addition, it presents a low electrical conductivity compared with graphene or carbon nanotubes, which makes it suitable for insulation layers and supporting materials in electronics and batteries (Ref 30, 31).

In this work, we provided an alternative method to fabricate free-standing ANF films by spin coating of ANF-based dispersions on the glass slide, which is much facile and able to tune the thickness of the films. The ANF films also showed intriguing multiple properties like Kevlar such as high mechanical properties (ultimate strength up to 182 MPa and ultimate

**Jing Lyu**, School of Materials Science and Engineering, Northwestern Polytechnical University, Xi'an 710072 Shaanxi, People's Republic of China; and Department of Chemical Engineering, University of Michigan, Ann Arbor, MI 48109; and **Lehao Liu**, **Xing Zhao**, **Yudong Shang**, **Tingkai Zhao**, and **Tiehu Li**, School of Materials Science and Engineering, Northwestern Polytechnical University, Xi'an 710072 Shaanxi, People's Republic of China. Contact e-mails: lehaoliu@163.com, liulehao@yahoo.com, litiehu@nwpu.edu.cn.

tensile strain up to 10.5%), high-temperature stability and chemical inertness.

## 2. Experimental

### 2.1 Materials and Chemicals

Bulk Kevlar 69 was purchased from Thread Exchange. Dimethyl sulfoxide (DMSO), potassium hydroxide (KOH), sodium hydroxide (NaOH) and hydrogen chloride (HCl) were all purchased from Sigma-Aldrich and used as-received. Deionized water (DI water 18.2 M $\Omega$ /cm) was obtained from a Millipore Milli-Q system. Glass slides (50 mm  $\times$  50 mm) were cleaned by piranha solution (3:1 v/v H<sub>2</sub>SO<sub>4</sub>:H<sub>2</sub>O<sub>2</sub>).

### 2.2 Preparation of ANF Films

ANF solution was synthesized according to the reference earlier (Ref 20). Specifically, 2.0 g bulk Kevlar 69, 2.0 g KOH and 98 g DMSO were put in a glass bottle and then sealed with a cap. The mixture was magnetically stirred at room temperature until a dark red, viscous ANF dispersion was formed. It would take 3 weeks to obtain the 2 wt.% ANF solution.

To fabricate the ANF films by spin coating, glass slides were cleaned with piranha solution, followed by thoroughly rinsing with DI water and compressed air-drying. After that, 3 mL ANF solution was dropped on the clean glass substrates and immediately spin-coated for 30 s. Spinning speeds were tuned to be 1000, 800, 600, 400 and 200 rpm to prepare the various films with different thickness, respectively. The ANF hydrogel was soon formed and then detached from the glass slides, when immersing the glass substrate-supported ANF films into DI water or ethanol. The formation of free-standing ANF films is attributed to the protonation of the ANFs and substitution of DMSO by DI water or ethanol (Ref 24). The ANF films were sandwiched between two polytetrafluoroethylene (PTFE) plates to dry at 80 °C for 24 h before characterizations and tests.

### 2.3 Characterizations and Tests

UV-Vis absorbance spectra were obtained by using an 8453 UV-Vis ChemStation spectrophotometer (Agilent Technologies). Transmission electron microscope (TEM) images were obtained by a JEOL JEM 3010. One drop of diluted solution (10  $\mu$ L) of ANFs was placed on the surface of a copper grid coated with carbon and dried at air before taking the TEM images. The morphologies of the ANF films were inspected with a Hitachi S-4800 scanning electron microscope. The thermal stability of the ANF films was determined by a TA Instruments Discovery Thermogravimetric Analyzer (TGA) with a temperature ramp to 700 °C at 10 °C/min in nitrogen or air atmosphere. The x-ray diffraction (XRD) analysis of the specimens was performed with a XRD-7000 (Shimadzu) diffractometer using a Cu K $\alpha$  radiation ( $\lambda = 0.15406$  nm). The XRD patterns of the ANF films were recorded in scanning range of 10°-80° with a step size of 0.02° s<sup>-1</sup>. Fourier transform infrared spectroscopy (FTIR) was performed on a Prestige-21 spectrophotometer to investigate the chemical properties of the ANF films. The testing range is between 1000 and 4000 cm<sup>-1</sup>. The thickness of the films was measured by a surface profiler (KLA-Tencor D-120) after drying the films on glass slides. As expected, the films adhered to the glass very

tightly. A few short cuts (< 10 mm in length) were made for each film before the test. Five to ten sets of data were collected to give the average thickness. The tensile behavior of each film was determined using a TA XT Plus Texture Analyzer (Stable Micro Systems) at a loading rate of 0.01 mm/s with a gage length of  $\sim$  10 mm. All samples were cut into rectangular strips of 2 mm in width using razor blades and five strips were measured for each film.

## 3. Results and Discussion

### 3.1 Characterizations of the ANF Films

Aramid fiber was chosen in this study because of the well-known dramatically high strength attributed to hydrogen bonding and radial orientation (Fig. 1a) and excellent thermal stability and chemical resistance. A dark red viscous solution was obtained by adding bulk Kevlar threads into DMSO solvent in the presence of KOH and stirring for 3 weeks (Fig. 1b inset). The average diameter of the ANFs after the dissolution of the bulk Kevlar fibers is  $\sim$  20 nm, and the lengths are several micrometers (Fig. 1b).

Spin coating, as one of the most widely used technique for obtaining uniform thin films, was employed to prepare ANF films. This process shows great versatility in controlling the thickness of the films via tuning the rotation speed and time. The ANF films with thickness of 3, 4, 5.5, 7.5 and 10  $\mu$ m are fabricated via adjusting the spinning speed to 1000, 800, 600, 400 and 200 rpm, respectively. As expected, the thin films (< 7.5  $\mu$ m) exhibit high transparency (Fig. 1c) owing to the diameter of ANFs markedly smaller than the wavelengths of visible light.

Free-standing composite films were obtained after protonation of ANFs and substitution of DMSO by water or ethanol, and the resulting films are denoted as ANF-water or ANF-ethanol. The SEM images (Fig. 2a, b) show the surface morphology of the ANF-water film after oven-drying. The high-magnification SEM image clearly demonstrates that the one-dimensional aramid nanofibers interconnected to form the two-dimensional ANF film with many nanoscaled pores. However, the ANF-ethanol film has many microsized pores with diameter of  $\sim$  10  $\mu$ m, because ethanol is a weaker proton donor (Fig. 2c, d). Since the properties of the nanomaterials are essentially determined by their microstructures, we can deduce that the ANF-water films with nanopores result in higher mechanical properties, while the ANF-ethanol films with micropores can enable high mass loading of large-sized fillers for obtain nanocomposites.

The UV-Vis spectra of both the ANF films showed an absorption peak at  $\sim$  335 nm, which is attributed to the polyamide structure of ANFs (Fig. 3a). To study the effects of the dissolution and protonation procedures on the chemical structure, FTIR spectra of the ANF films were obtained (Fig. 3b). The absorption peaks of the ANF films were observed at 3326, 1650, 1545 and 1516 cm<sup>-1</sup>, which are ascribed to N-H stretching vibrations, C=O stretching vibrations, N-H deformation and C=C stretching vibrations, respectively. Compared with the Kevlar threads, both the ANF films showed higher absorbance intensities at 3326 and 1650 cm<sup>-1</sup>, which indicates that the protonation process might induce the formation of amines and carboxylic acids. Moreover,



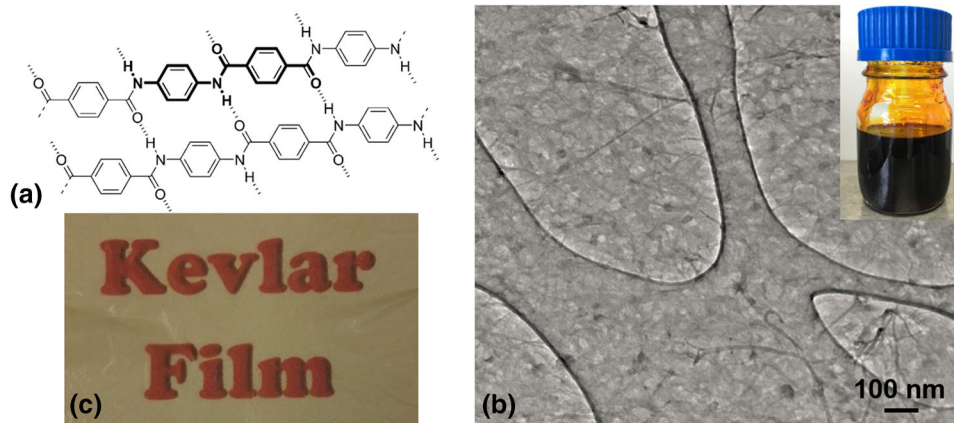


**Fig. 1** (a) Molecular structure of aramid fibers. (b) TEM image of ANFs. Inset: photograph of 2 wt.% ANF solution. (c) Photograph of the transparent ANF film

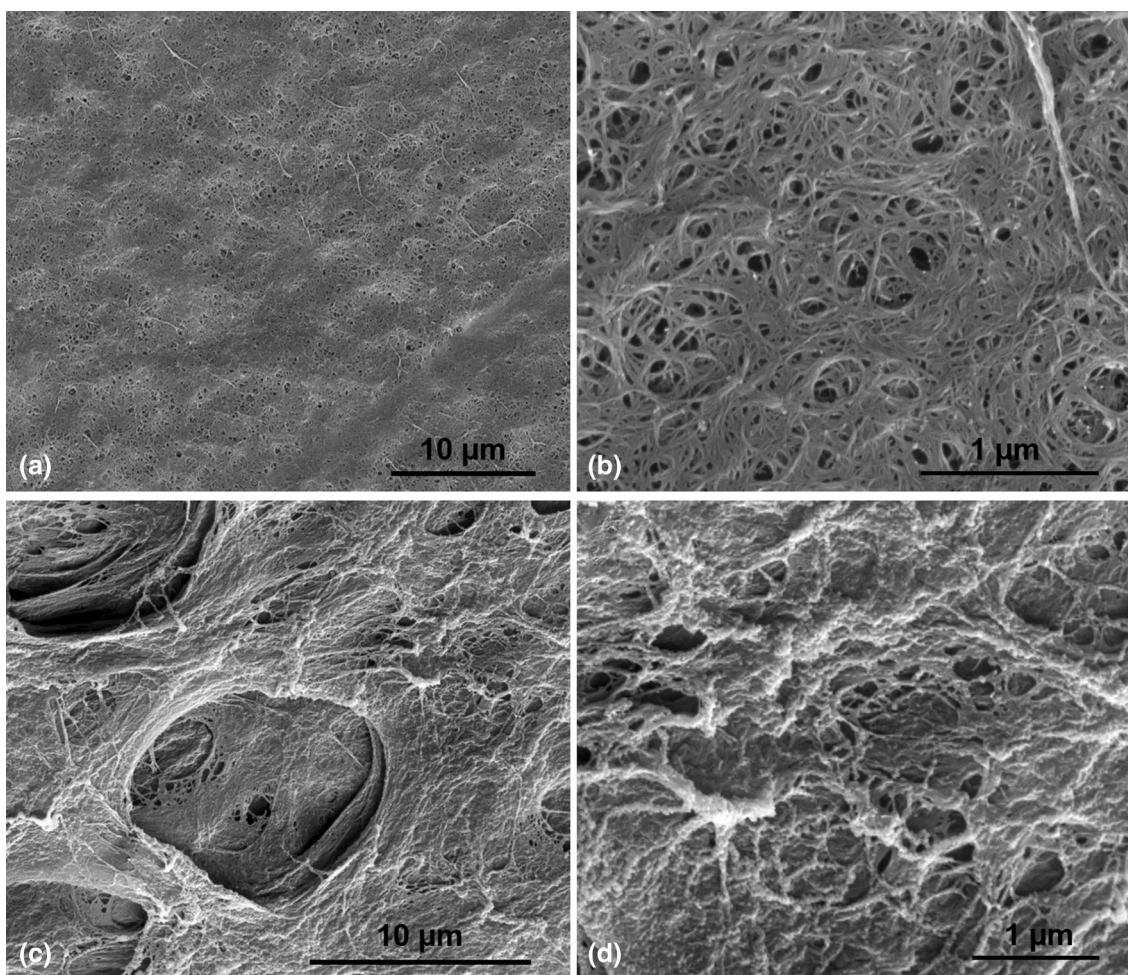


**Fig. 2** SEM images of the ANF-water films (a, b), and ANF-ethanol films (c, d)

the absorbance intensities at  $2926$  and  $2856\text{ cm}^{-1}$  decreased for both the ANF films, due to the broader distribution of the bond lengths and surface states of the ANFs.

The x-ray diffraction (XRD) measurements show broadening of characteristic Kevlar peaks from  $18^\circ$  to  $30^\circ$  for both the ANF-water and ANF-ethanol films (Fig. 4a). The XRD pat-

terns also indicate that the dissolution process did not change the structure of the nanofibers. To investigate the thermal stability of ANF films, TGA curves of the ANF films were measured under nitrogen and air atmosphere, respectively. The degradation started from  $\sim 550^\circ\text{C}$  under  $\text{N}_2$  atmosphere and  $500^\circ\text{C}$  in air (Fig. 4b), indicating that the ANF films exhibited

extraordinary thermal resistance similar to the bulk ANF threads (Ref 32). This is very important because thermal stability is necessary for wide applications of the polymer films.

### 3.2 Mechanical Properties of the ANF Films

Spin coating shows great versatility in controlling the thickness of the films via tuning the rotation speed, so we investigated the mechanical properties of the ANF films as a function of spin coating speed. Figure 5 illustrates the stress-strain curves for the ANF-water and ANF-ethanol films. When the rotation speed decreased from 1000 to 200 rpm, the ultimate strain of the ANF-water films increased from 7.2 to 15.6% due to the gradual increase of the films thickness. The results indicated that the ANF films fabricated via spin coating exhibited superior tensile strain to the films obtained by layer-by-layer or vacuum-assisted flocculation (Ref 33), which may be attributed to the porous structures. Meanwhile, the ultimate stress increased when the speed decreased from 1000 to 600 rpm, but decreased when the speed decreased from 600 to 200 rpm, due to the uneven films formed under low spin speed. The films prepared at 600 rpm showed the optimal mechanical properties with a tensile strength of 182 MPa and a strain of 10.5%. Compared with ANF-water films, these ANF-ethanol

films exhibit similar trends but lower ultimate strengths and strains (strength of 138 MPa and a strain of 5.8% at 600 rpm). Such results indicated that the ANF-water films resulted in a better mechanical performance, which is ascribed to the more uniform structure with smaller pores (Fig. 2).

### 3.3 Finite Element Modeling for Mechanical Simulations

ANSYS is a common finite element modeling (FEM) software for strain and stress simulations. It can not only calculate the average strain and stress in the film, but also give the strain along a specified axis. The material properties of the ANF films for the FEM were obtained from the tensile tests of the ANF-water and ANF-ethanol films (Table 1). We performed uniaxial tension experiments on the ANF films with a rigid boundary condition applied to the bottom.

Figure 6 presents the von Mises strain distribution of the ANF-water and ANF-ethanol films induced by the 5% applied strain ( $\epsilon = 5\%$ ), and the ANF-water films at 10% applied strain ( $\epsilon = 10\%$ ). The highest values of strain were observed at the four corners of the rectangular strips which were restricted rotation or displacement on  $x$  or  $z$  direction, while the strain is distributed uniformly throughout the center of the specimen. At 10% applied strain, the distribution of the von Mises strain in

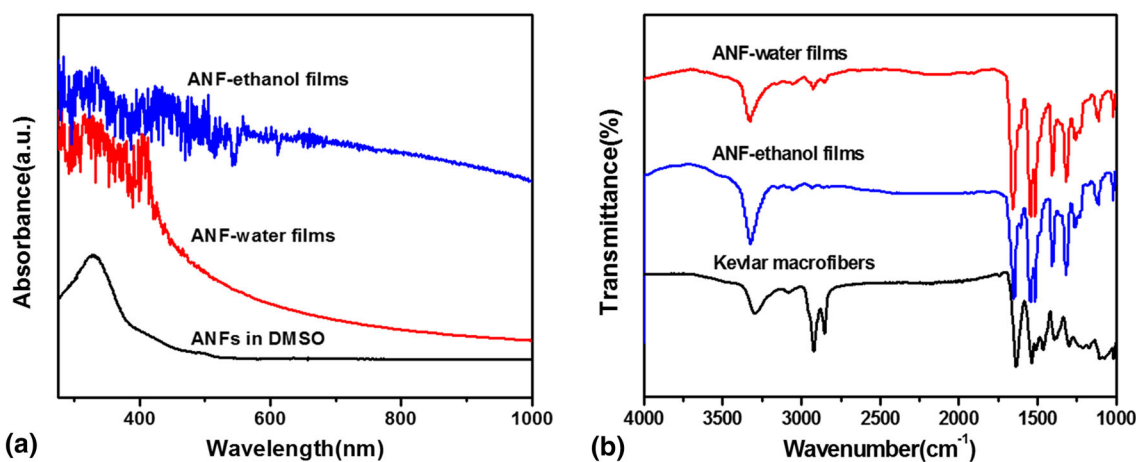


Fig. 3 (a) UV-Vis spectra of ANF solution in DMSO, ANF-water films and ANF-ethanol films. (b) FTIR spectra of Kevlar fibers, ANF-water films and ANF-ethanol films

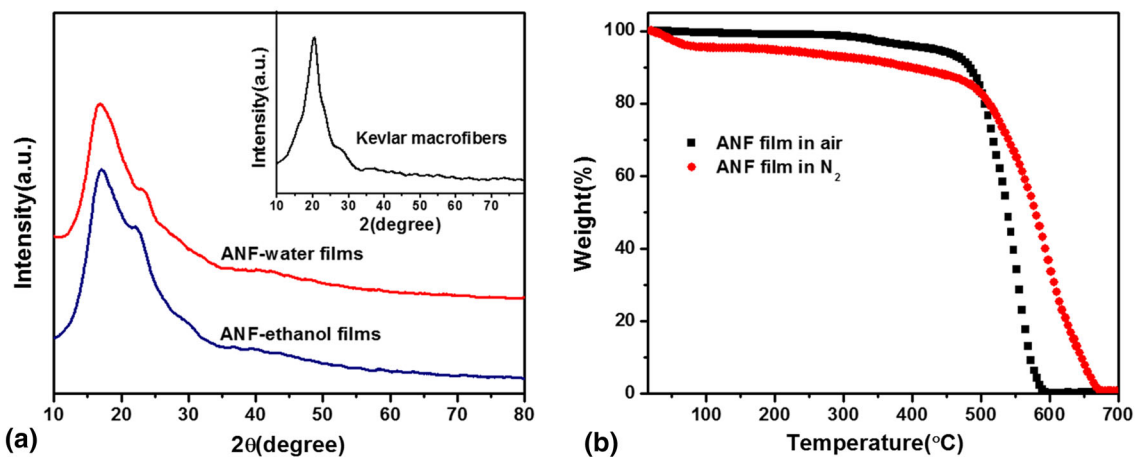


Fig. 4 (a) XRD patterns of the ANF-water and ANF-ethanol films. Inset: XRD pattern of the Kevlar fibers. (b) TGA curves of the ANF films tested in air and N<sub>2</sub>, respectively

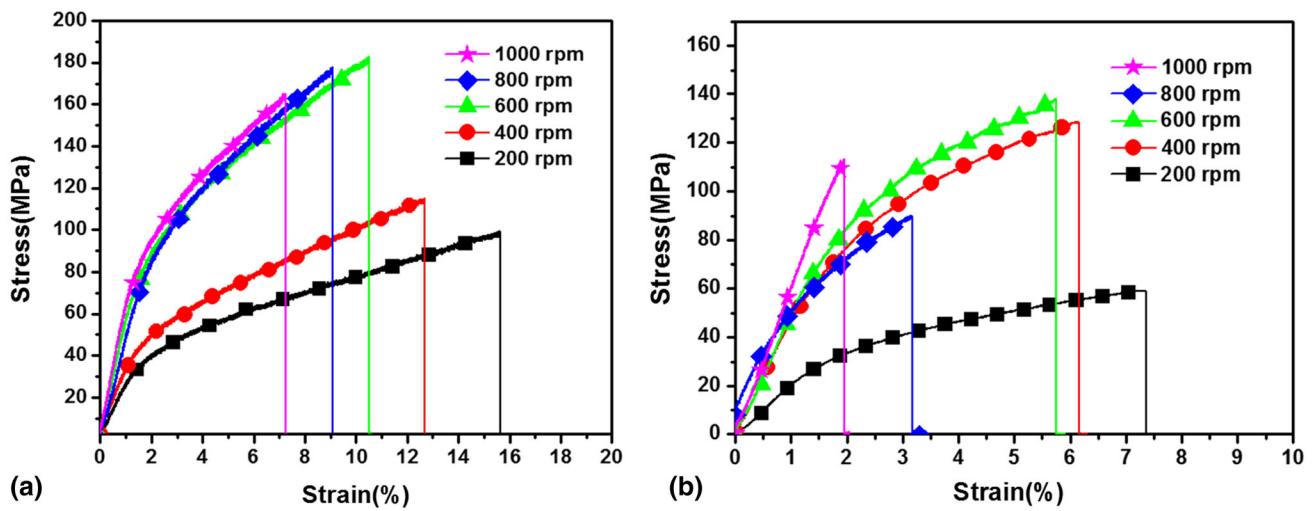


Fig. 5 Stress-strain curves for the ANF-water films (a) and ANF-ethanol films (b) with different spin coating speed

Table 1 Element type and material properties of the ANF-water and ANF-ethanol films for the FEM

Sample type	Element type	Thickness, $\mu\text{m}$	Young's modulus, GPa	Poisson's ratio
ANF-water films	Shell 181	5.5	4.5	0.3
ANF-ethanol films	Shell 181	5.5	5.1	0.3

5% applied strain (ANF-water and ANF-ethanol films)

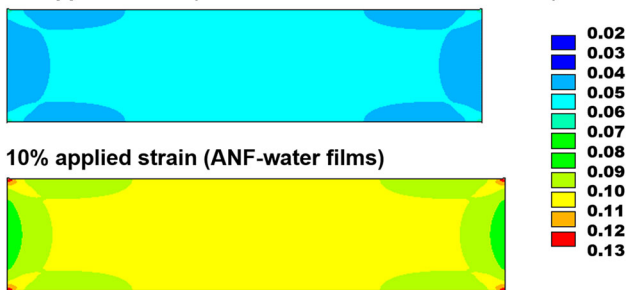


Fig. 6 FEM of von Mises strain distribution for 5% applied strain on the ANF-water and ANF-ethanol films, and 10% applied strain on the ANF-water films

5% applied strain (ANF-water films)

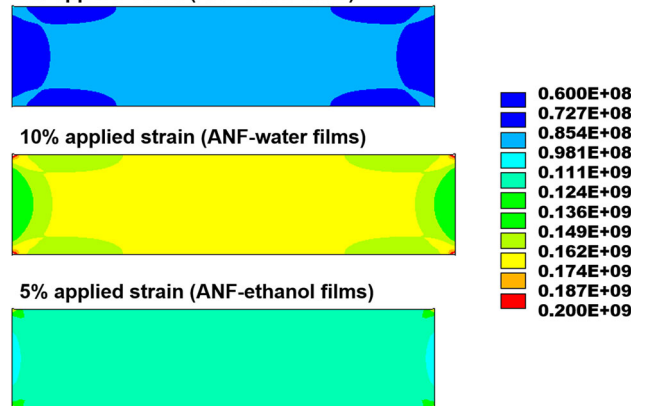


Fig. 7 FEM of von Mises stress distribution for 5 and 10% applied strain on the ANF-water films, and 5% applied strain on ANF-ethanol films

the ANF-water film was similar to that of 5% applied strain except the higher overall strain, which is in accordance with the experimental results (Fig. 5a).

Figure 7 displays the von Mises stress distributions in the ANF-water films at an applied strain of 5 and 10%, and the ANF-ethanol films at an applied strain of 5%, which is well within the regime of the deformation. The simulations reveal that a lower applied strain leads to a lower stress, which is accordant with the von Mises strain simulation. Furthermore, under the same applied strain ( $\epsilon = 5\%$ ), the von Mises stress of the ANF-water films is lower than that of the ANF-ethanol films due to the smaller Young's modulus value of the ANF-water films. Briefly, both the experimental data and simulation results are consistent with each other.

### 3.4 Chemical Stability

In order to evaluate the chemical resistance, both the ANF-water and ANF-ethanol films prepared at 600 rpm were

immersed in 1 M NaOH and HCl solutions for 24 h, respectively. After drying, tensile tests were applied to study the mechanical properties of the films (Fig. 8). The ANF-water films after the NaOH treatment remained an ultimate tensile strength of 172 MPa and a strain of 10.4%. While after HCl treatment, the films showed an ultimate tensile strength of 169 MPa and a strain of 10.5%. These values are comparable to those of the pristine ANF-water films (a tensile strength of 182 MPa and a strain of 10.5%), indicating that the ANF films exhibit outstanding chemical inertness against the acidic and alkaline corrosion. In addition, the ultimate tensile strength and strain of the ANF-ethanol films almost kept the same with or without chemical treatments.



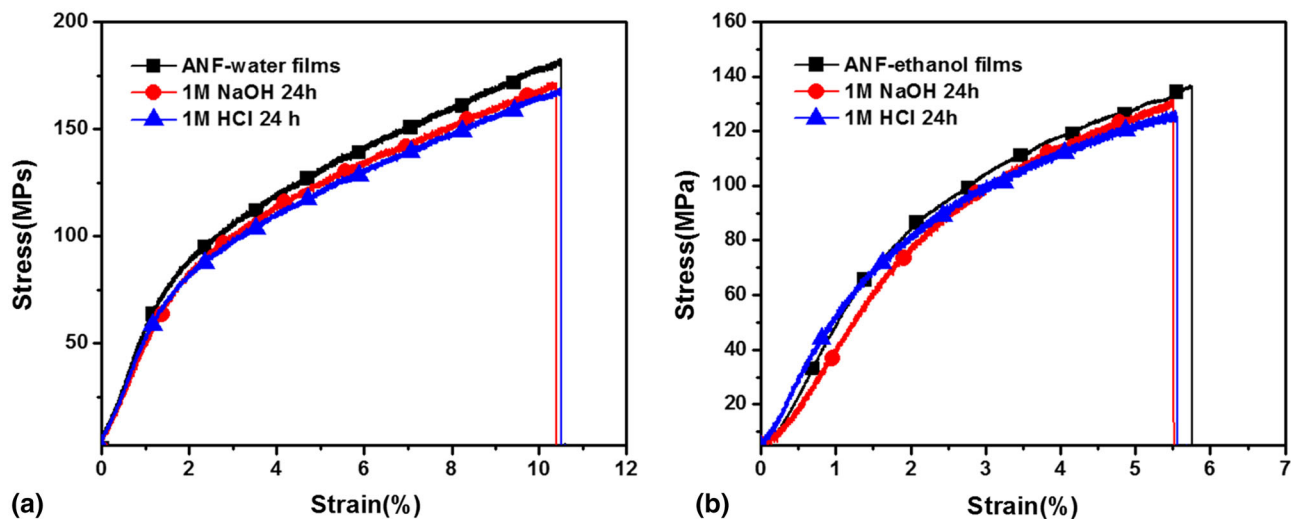


Fig. 8 Stress-strain curves of the pristine and chemically treated ANF-water films (a) and ANF-ethanol films (b)

## 4. Conclusions

We facilely prepared ANF films with various thicknesses by spin coating an ANF DMSO solution under different rotation rate. Mechanical tests indicated that the ANF-water films showed an ultimate tensile strength of 182 MPa and a strain of 10.5%, which are both higher than those of the ANF-ethanol films (a strength of 138 MPa and a strain of 5.8%). This is attributed to the more uniform dispersion of the ANFs in the ANF-water films than in the ANF-ethanol films. The tensile strength and strain distributions were simulated with the finite element modeling, and the simulated stress and strain distributions are consistent with the experimental data. The ANF films also exhibited high thermal stability with the high decomposition temperatures ( $\sim 550$  °C under  $N_2$  atmosphere and 500 °C in air). Moreover, the films showed outstanding chemical inertness against acid and alkali corrosion. The simple method demonstrated here provides an important way to prepare high-performance ANF films for designing new composite systems.

## Acknowledgments

This work was supported by the Specialized Research Fund for NSF of China (51172184, 51572221), China Aeronautical Science Fund (2014ZF53074), and Specialized Research Fund for the Doctoral Program of the Ministry of Education (20116102110014).

## Conflict of interest

The authors declared no potential conflicts of interest with respect to the research, authorship and/or publication of this article.

## References

1. F. Xu and Y. Zhu, Highly Conductive and Stretchable Silver Nanowire Conductors, *Adv. Mater.*, 2012, **24**, p 5117–5122
2. M. Park, J. Im, M. Shin, Y. Min, J. Park, H. Cho, S. Park, M.-B. Shim, S. Jeon, D.-Y. Chung, J. Bae, U. Jeong, and K. Kim, Highly Stretchable

- Electric Circuits from a Composite Material of Silver Nanoparticles and Elastomeric Fibres, *Nat. Nanotechnol.*, 2012, **7**, p 803–809
3. C. Yan, X. Wang, M. Cui, J. Wang, W. Kang, C.Y. Foo, and P.S. Lee, Stretchable Silver-Zinc Batteries Based on Embedded Nanowire Elastic Conductors, *Adv. Energy Mater.*, 2014, **4**, p 1–6
4. C. Yu, C. Masarapu, J. Rong, B. Wei, and H. Jiang, Stretchable Supercapacitors Based on Buckled Single-Walled Carbon Nanotube Macrofilms, *Adv. Mater.*, 2009, **21**, p 4793–4797
5. K.S. Khare, F. Khabaz, and R. Khare, Effect of Carbon Nanotube Functionalization on Mechanical and Thermal Properties of Cross-Linked Epoxy-Carbon Nanotube Nanocomposites: Role of Strengthening the Interfacial Interactions, *ACS Appl. Mater. Interfaces*, 2014, **6**, p 6098–6110
6. S. Araby, Q. Meng, L. Zhang, H. Kang, P. Majewski, Y. Tang, and J. Ma, Electrically and Thermally Conductive Elastomer/Graphene Nanocomposites by Solution Mixing, *Polymer*, 2014, **55**, p 201–210
7. J.S.M. Zanjani, B. Saner Okan, Y.Z. Menceloglu, and M. Yildiz, Design and Fabrication of Multi-walled Hollow Nanofibers by Triaxial Electrospinning as Reinforcing Agents in Nanocomposites, *J. Reinf. Plast. Compos.*, 2015, **34**, p 1273–1286
8. S. Mallakpour and F. Sirous, Polymer Nanocomposites Containing *N*-Trimellitylimido-L-Phenylalanine Dicarboxylic Acid Moieties Reinforced with  $\alpha$ - $Al_2O_3$  Nanoparticles Modified with Citric Acid: Synthesis and Characterization, *Polym. Plast. Technol. Eng.*, 2015, **54**, p 532–540
9. N.-M. Florea, A. Lungu, E. Vasile, and H. Iovu, The Influence of Nanosilica Functionalization on the Properties of Hybrid Nanocomposites, *High Perform. Polym.*, 2012, **25**, p 61–69
10. E.T. Thostenson, W.Z. Li, D.Z. Wang, Z.F. Ren, and T.W. Chou, Carbon Nanotube/Carbon Fiber Hybrid Multiscale Composites, *J. Appl. Phys.*, 2002, **91**, p 6034–6037
11. S.K. Yadav and J.W. Cho, Functionalized Graphene Nanoplatelets for Enhanced Mechanical and Thermal Properties of Polyurethane Nanocomposites, *Appl. Surf. Sci.*, 2013, **266**, p 360–367
12. L.C. Tang, Y.J. Wan, D. Yan, Y.B. Pei, L. Zhao, Y.B. Li, L. Bin Wu, J.X. Jiang, and G.Q. Lai, The Effect of Graphene Dispersion on the Mechanical Properties of Graphene/Epoxy Composites, *Carbon*, 2013, **60**, p 16–27
13. L. Banks-Sills, D.G. Shiber, V. Fourman, R. Eliasi, and A. Shlayer, Experimental Determination of Mechanical Properties of PMMA Reinforced with Functionalized CNTs, *Compos. Part B*, 2016, **95**, p 335–345
14. E.D. Cranston, M. Eita, E. Johansson, J. Netrval, M. Salajková, H. Arwin, and L. Wagberg, Determination of Young's Modulus for Nanofibrillated Cellulose Multilayer Thin Films Using Buckling Mechanics, *Biomacromolecules*, 2011, **12**, p 961–969
15. C.K. Chu and Y.L. Chen, Ballistic-Proof Effects of Various Woven Constructions, *Fibres Text.*, 2010, **83**, p 63–67
16. T.J. Singh and S. Samanta, Characterization of Kevlar Fiber and Its Composites: a Review, *Mater. Today Proc.*, 2015, **2**, p 1381–1387

17. D. Tanner, J.A. Fitzgerald, and B.R. Phillips, The Kevlar Story—An Advanced Materials Case Study, *Angew. Chemie Int. Ed.*, 1989, **28**, p 649–654
18. F. Guo, Z.-Z. Zhang, W.-M. Liu, F.-H. Su, and H.-J. Zhang, Effect of Plasma Treatment of Kevlar Fabric on the Tribological Behavior of Kevlar Fabric/Phenolic Composites, *Tribol. Int.*, 2009, **42**, p 243–249
19. T.K. Lin, S.J. Wu, J.G. Lai, and S.S. Shyu, The Effect of Chemical Treatment on Reinforcement/Matrix Interaction in Kevlar-Fiber/Bismaleimide Composites, *Compos. Sci. Technol.*, 2000, **60**, p 1873–1878
20. M. Yang, K. Cao, L. Sui, Y. Qi, J. Zhu, A. Waas, E.M. Arruda, J. Kieffer, M.D. Thouless, and N.A. Kotov, Dispersions of Aramid Nanofibers: a New Nanoscale Building Block, *ACS Nano*, 2011, **5**, p 6945–6954
21. J. Fan, J. Wang, Z. Shi, S. Yu, and J. Yin, Kevlar Nanofiber-Functionalized Multiwalled Carbon Nanotubes for Polymer Reinforcement, *Mater. Chem. Phys.*, 2013, **141**, p 861–868
22. R. Sa, Y. Yan, Z. Wei, L. Zhang, W. Wang, and M. Tian, Surface Modification of Aramid Fibers by Bio-inspired Poly(dopamine) and Epoxy Functionalized Silane Grafting, *ACS Appl. Mater. Interfaces*, 2012, **6**, p 21730–21738
23. B. Park, W. Lee, E. Lee, S.H. Min, and B.S. Kim, Highly Tunable Interfacial Adhesion of Glass Fiber by Hybrid Multilayers of Graphene Oxide and Aramid Nanofiber, *ACS Appl. Mater. Interfaces*, 2015, **7**, p 3329–3334
24. K. Cao, C.P. Siepermann, M. Yang, A.M. Waas, N.A. Kotov, M.D. Thouless, and E.M. Arruda, Reactive Aramid Nanostructures as High-Performance Polymeric Building Blocks for Advanced Composites, *Adv. Funct. Mater.*, 2013, **23**, p 2072–2080
25. M. Yang, K. Cao, B. Yeom, M. Thouless, A. Waas, E.M. Arruda, and N.A. Kotov, Aramid Nanofiber-Reinforced Transparent Nanocomposites, *J. Compos. Mater.*, 2015, **49**, p 1873–1879
26. Q. Kuang, D. Zhang, J.C. Yu, Y. Chang, M. Yue, Y. Hou, and M. Yang, Towards Record-High Stiffness in Polyurethane Nanocomposites Using Aramid Nanofibers, *J. Phys. Chem. C*, 2015, **119**, p 27467–27477
27. J. Fan, Z. Shi, L. Zhang, J. Wang, and J. Yin, Aramid Nanofiber-Functionalized Graphene Nanosheets for Polymer Reinforcement, *Nanoscale*, 2012, **4**, p 7046–7055
28. M. Lian, J. Fan, Z. Shi, H. Li, and J. Yin, Kevlar<sup>®</sup>-Functionalized Graphene Nanoribbon for Polymer Reinforcement, *Polymer*, 2014, **55**, p 2578–2587
29. J. Fan, Z. Shi, M. Tian, and J. Yin, Graphene–Aramid Nanofiber Nanocomposite Paper with High Mechanical and Electrical Performance, *RSC Adv.*, 2013, **3**, p 17664
30. S.-O. Tung, S. Ho, M. Yang, R. Zhang, and N.A. Kotov, A Dendrite-Suppressing Composite Ion Conductor from Aramid Nanofibres, *Nat. Commun.*, 2015, **6**, p 6152
31. S. Hu, S. Lin, Y. Tu, J. Hu, Y. Wu, G. Liu, F. Li, F. Yu, and T. Jiang, Novel Aramid Nanofiber-Coated Polypropylene Separators for Lithium Ion Batteries, *J. Mater. Chem. A.*, 2016, **4**, p 3513–3526
32. X. Li and M. Huang, Thermal Degradation of Kevlar Fiber by High-Resolution, *J. Appl. Polym. Sci.*, 1999, **4**, p 565–571
33. J. Zhu, W. Cao, M. Yue, Y. Hou, J. Han, and M. Yang, Strong and Stiff Aramid Nanofiber/Carbon Nanotube Nanocomposites, *ACS Nano*, 2015, **9**, p 2489–2501